

Magneto-Optical Study High-Purity Niobium for Superconducting RF Application

A. A. Polyanskii, P. J. Lee, A. Gurevich, Zu-Hawn Sung and D. C. Larbalestier

The National High Magnetic Field Laboratory, Florida State University, 1800 E. Paul Dirac Drive, Tallahassee, FL 32310, USA

Abstract. In this review we present a summary of our recent Magneto-Optical (MO) imaging of high-purity Nb for SRF cavity application. Superconducting RF cavities have been chosen as the accelerating technology for the International Linear Collider, and it is of vital importance to understand the limiting factors to the performance of these devices. We have been using a combination of MO, imaging, magnetization measurements and a variety of non-contact surface topology measurement techniques to characterize samples of high purity Nb supplied by Fermi National Accelerator Laboratory (FNAL) and Thomas Jefferson National Accelerator Facility (TJNAF). Localized non-uniformities in the superconducting properties were revealed on samples which were cut from rolled polycrystalline sheets (FNAL) and subjected to buffered chemical polishing (BCP) and heat treatments (HT) steps designed to simulate typical SRF cavity production. MO examination of the polycrystalline Nb sheets in perpendicular and in-plane fields reveals the perturbations in the critical currents caused by topological defects such as the steps between adjacent grains produced by BCP. MO examination of bi-crystals prepared from a disc cut directly from a very large grain size ingot (manufactured for TJNAF by CBMM) showed preferential flux penetration at grain boundaries for bi-crystal samples in which the GB interface was almost parallel to the externally applied field. This result was the first direct evidence of depressed superconductivity at GBs. By developing an understanding of how and why such behavior occurs, we hope to be able to improve the properties of cavity accelerators.

Keywords: SRF, niobium, magneto-optical, magnetic flux

PACS: 74.25.Wx

INTRODUCTION

In the framework of the R&D effort in support of the future International Linear Collider (ILC) project, we are studying the superconducting properties of pure Nb for SRF cavities using Magneto-Optics, magnetization and surface analysis. Magnetization and MO measurements reveal how and where magnetic vortices penetrate the Nb [1-3]. An understanding of what degrades the performance of high purity Nb used for SRF cavity fabrication is vital to the success of the ILC. In recent years it has become clear that the performance of superconducting Nb cavities for RF application is very sensitive to Nb surface quality, and surface preparation by buffered chemical polishing [4, 5] or by electropolishing [6, 7] followed by a low temperature bake is vital [8]. This is important since the penetration of small numbers of flux lines into the cavity surface during RF operation is a possible mechanism for causing Q-drop or quenching. Gurevich [9, 10] has recently proposed a model for Q-drop

triggered by early flux penetration, which makes local study of flux penetration very appropriate.

In this paper we review our recent results on pure polycrystalline Nb samples taken through typical cavity optimization process and results on samples from Nb sheet with extremely big grains. We were able to study influence of separate grain boundaries on flux behavior. Major differences between the conditions currently possible in MO compared with SRF cavity operation are the use of a DC rather than RF field and temperatures down to 5 K rather than 2 K.

EXPERIMENTAL TECHNIQUE

Description of the Samples

Polycrystalline Nb Sheet

FNAL supplied polycrystalline Nb sheet samples taken at each step of a simulated cavity production process. In addition to “regular” sheet samples, a series was taken in a “welded” region. The Nb grains in the “regular” samples in the as-received condition were approximately 50 μm in cross-sectional diameter, while the weld regions after an e-beam weld included grains larger than 1 mm grown during the melting of the material during welding. The specific features of the weld samples were steps at grain boundaries and machinery marks. The samples from both regions were approximately $2.75 \times 2.75 \times 1.5$ mm in dimension.

The cavity optimization process for regular and welded samples includes these 5 steps:

- (1) cold work produced by the sample machining process, followed by degreasing,
- (2) ~ 100 μm BCP etch,
- (3) 5 hours at 750°C in a vacuum $< 10^{-6}$ Torr,
- (4) ~ 20 μm BCP etch and
- (5) 50 hours at 120°C in a vacuum $< 10^{-6}$ Torr.

As mentioned above, the preparation steps comprised of two BCP (1:1:2) etching stages and high (~ 700 -800 °C) as well as low (120 °C) temperature heat treatment (bake). The first etching step removes ~ 100 μm and with it the mechanical defects introduced into the surface by rolling and wire erosion cutting or machining. The high temperature heat treatment serves to outgas the hydrogen introduced into the material by the etching and to anneal the previously work-hardened material. The second, light etching step is intended to remove the surface contamination introduced by the HT. The final, low temperature heat treatment serves to emulate the so-called “baking”, which is known to improve the high field SRF cavity performance. Rinsing with ultra-pure water and drying with filtered nitrogen, was performed in a class 1000 clean-room at FNAL. The samples were transported in polyethylene tubes containing dry nitrogen as buffer gas. The exposure of the samples to external atmosphere, especially following the heat treatment was thus kept to a minimum.

We characterized both polycrystalline sample sets in each condition by both MO (see Figs. 3-5) and magnetization using a vibration sample magnetometer (VSM), both measurements being performed at 7 K. This temperature was chosen so that the

applied field in the MO cryostat could exceed the upper critical field (H_{c2}) of our samples (for pure Nb at 7 K, $H_{c2} \sim 110$ mT) [11].

Very Large Grain Size Nb Sheet

In this study we were able also to use large bi-crystal and tri-crystal samples cut from slice of one of the CBMM extremely large-grain billets fabricated for Jefferson Laboratory (TJNAF) [12]. The Nb sheet was given sufficient BCP treatment at TJNAF to reveal the grain boundary locations. The reverse side was in the rough-cut condition, which necessitated further mechanical polishing followed by etching so that we could determine the locations of the boundaries after traversing the thickness of the slice.

Rectangular cross-section samples were cut from the 1.8 mm thick Nb sheet by diamond saw. Samples varied from 1.5 to 2 mm in width and 2 to 3 mm in length. For MO measurements we were able to reduce sample thickness by slicing the 1.8 mm samples in two, yielding two sub-1 mm thick sections. Then a cut face was polished, sufficiently to see the GB location. The disc-shape samples were cut from sheet by electroerosion with final size after BCP the 3.3 mm in diameter and 1.78 mm thick.

After the initial investigation suggested the flux penetration may be sensitive to the angular alignment of the grain boundary, a bi-crystal that had not shown penetration in the earlier investigation was selected to be rotated 90° so that its grain boundary was parallel to the applied field.

Description of Magneto-Optical Imaging Technique

A schematic illustration of the magneto-optical (MO) setup is presented in Fig. 1 a, b and is described in detail in [13]. The technique uses the strong magneto-optical Faraday Effect in garnet film doped by Bi to measure the vertical component of the magnetic field above the sample. The spatial resolution attained is $\sim 5 \mu\text{m}$ when the garnet is placed directly on the well polished face of the sample and fields of ~ 1 mT can be resolved. A continuous flow cryostat permits sample temperatures down to ~ 5 K. Two external electromagnetic solenoids can apply vertical (Hz) and in-plane (Hx) fields up to ~ 120 mT to the sample. The field enhancement (Fig.1c), due to the rectangular cross-section of most of our samples, in the diamagnetic state is considerable, rising to a maximum field at the mid-point of each edge of the rectangle. As calculated using finite element analysis, the enhancement may be about 2.7-10 times higher than external field and depend on the sample size.

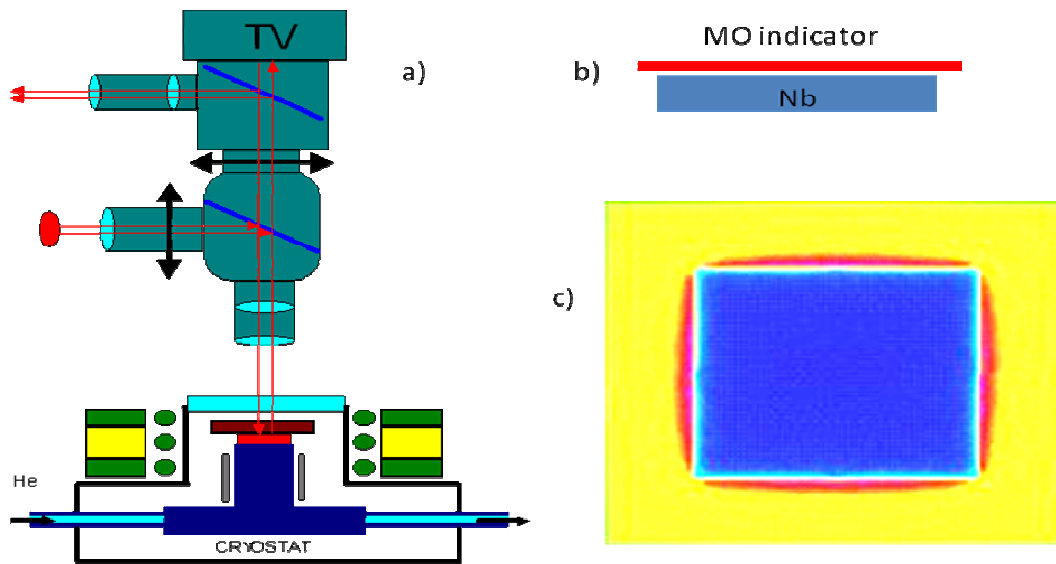


FIGURE 1. a) Magneto-optical setup, b) geometry of Magneto-Optical experiment, c) enhancement of external field at the center of each side rectangular Nb when it is fully diamagnetic.

Fig. 2 contrasts the magnetic flux behavior in pure Nb rectangular cross-section and circular cross-section samples. The field enhancement factor produces the characteristic “rooftop” field penetration pattern in a rectangular sample during ZFC regime (Fig. 2a) e.g. flux penetrates much faster at the mid-point of each edge. For the disk-shaped sample the enhancement is the same everywhere along its perimeter (Fig 2c). The trapped magnetic field in Fig. 2b and 2d after cool down in external field (FC) associated with bulk screening current flows along perimeters. The 90° turn of the screening current at the diagonals produces sharp and symmetrical “rooftop” pattern in these pure Nb samples, indicative of homogenous bulk properties.

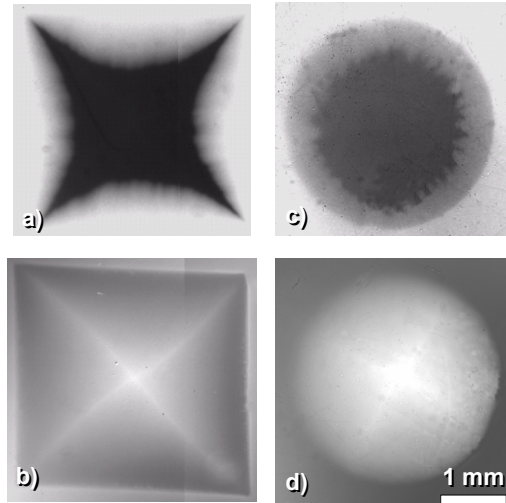


FIGURE 2. Magneto-optical images at $T = 6$ K rectangular a, b) and disc-shape c, d) Nb taken in ZFC a) $H=120$ mT, c) $H=42$ mT and FC b), d), when $H=120$ mT reduced to zero.

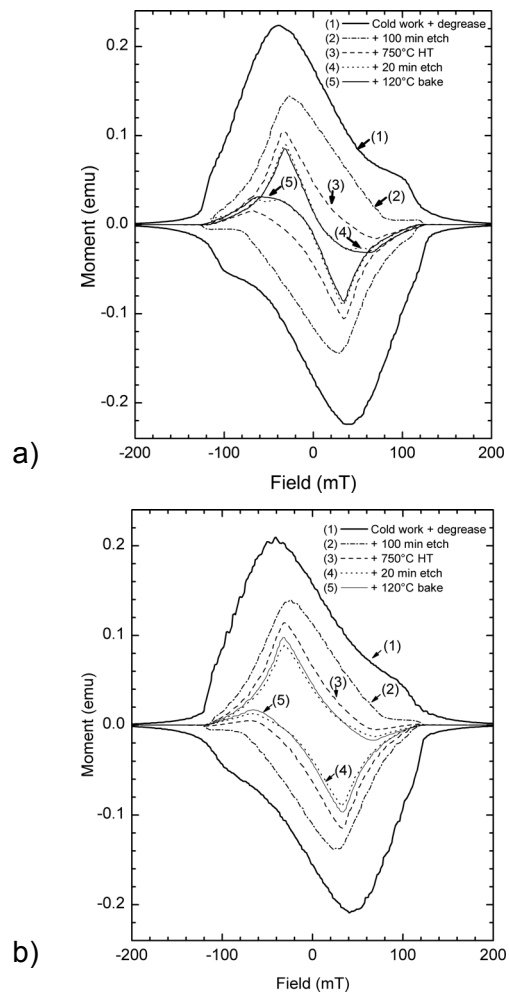


FIGURE 3. Magnetization curves taken at 7 K on a) large-grain weld samples and b) on fine-grain.

RESULTS

Polycrystalline Nb Sheet

Using MO and the VSM we characterized the local and global magnetization polycrystalline Nb with regular and big grain sizes (weld samples) at each stage of processing associated with cavity production route [3]. Fig. 3 presents VSM magnetization measurements on weld and regular samples after each step in the cavity optimization process. In the magnetization experiment, an external field was also applied perpendicular to the wide face of each sample. Magnetization hysteresis is significantly reduced by the 100 μm BCP etch (curve 2), further reduced by the 750 $^{\circ}\text{C}$ heat treatment (curve 3) and the subsequent etch (curve 4), but the final bake does not change the hysteresis for either the regular or weld samples. The removal of the cold work by the etch treatment (curve 2) is indicated by the large reduction in H_{c2} and by a small increase in the field of first flux penetration, approximately H_{c1} as the Ginzburg-Landau parameter κ is lowered to its annealed value found in the sheet center. The magnetization hysteresis cannot be unambiguously associated with either surface or bulk pinning from observing the global magnetization curves but MO imaging of the same sample can help elucidate the different contributions.

Figures 4 and 5 present a summary of a much larger image set taken at many fields for all regular and weld samples along the processing route. Optical images clearly show coarse surface machining marks (row 1) that are somewhat smoothed after the BCP etching (conditions 2 and 4) for the small-grain, regular samples but are retained throughout processing in the weld samples. MO images taken at 7 K are shown in rows 2-4.

Row 4 in figures 4 and 5 show field cooled (FC) images. Evidence about the bulk pinning component of the hysteresis may be deduced from the images (row 4) made after cooling the samples in a field of 120 mT from above T_c to 7 K. The samples are then completely penetrated by field but, as the samples cool, defects capable of pinning flux become stronger and permit a bulk current density. Reducing the external field to zero at 7 K then establishes a roof pattern associated with such bulk screening current flow. Figs. 4 and 5 taken in field cooled (FC) regime show quite strong rooftop patterns after steps 1 and 2, which progressively fade away through step 5. We interpret this weakening of the roof-top-pattern as showing that the bulk pinning component of the hysteresis is progressively reduced through the whole optimization sequence. Rather symmetric roof patterns are seen in the FC images of row 4, consistent with the hysteresis shown in Fig. 3, even in conditions 4 and 5. As mentioned above the symmetric rooftop patterns indicate homogenous bulk properties.

Evidence on the influence of the surface condition on flux penetration is better derived from MO images in the increasing field e.g. zero field-cooled (ZFC) regime. In all cases these images in rows 2 and 3 are less uniform after HT (step 3) than the remanent images shown in row 4. The flux jumps into samples suddenly and dendritic instability well visible on MO images. The regular samples in Fig. 5 do show the expected tendency for flux to enter along the centerline of each face where the field enhancement is greatest. Comparing the lower field ZFC images in row 2 (set 3-5) to

higher field images in row 3, it can also be seen that the pattern does become more regular after more flux has entered.

The weld samples show generally similar unstable behavior with two special features. The ZFC field images show distinctly non-uniform penetration after steps (1) and (2). After the 750°C heat treatment, flux penetration for fields just above H_{c1} ($H_{ext} \sim 30$ mT) becomes markedly more variable. Sudden and massive flux penetration from the center of each face is indicated in the sample 4 and 5 images, consistent both with the fact that the peak in the magnetization loops occurs at ~ 30 mT and that there is little bulk pinning to inhibit flux entry.

These significant changes in the MO images are particularly strong after the 20 min etch in step (4). This second chemical etch, which is believed to cause topological defects like grooves or steps between adjacent grains promotes flux entry in the large grain weld samples, as can be seen by comparing the MO and optical images. The grain boundaries visible in the MO images of the weld samples after steps 4 and 5 are direct evidence that the flux profile is being perturbed by the grain structure. Some perturbations to the FC MO images of the treatment 4 and 5 weld samples are consistent with perturbed properties of one or more of the Nb grains that are clearly visible in the optical and ZFC images.

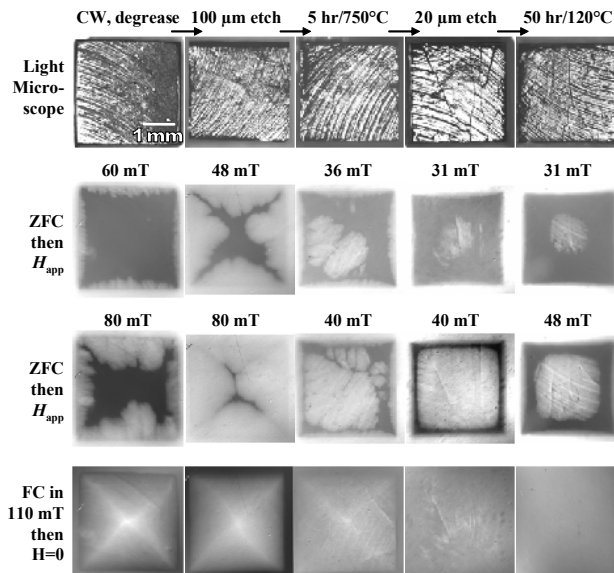


FIGURE 4. Reflected light and magneto-optical images of the weld (large grains) samples, taken sequentially after each process step. MO images were taken in the stated perpendicular external field [3].

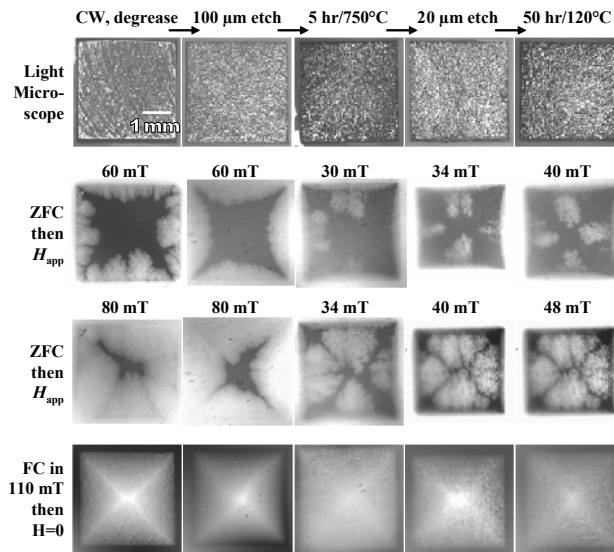


FIGURE 5. Reflected light and magneto-optical images of the regular (small grains) samples, taken sequentially after each process step. MO images were taken in the stated perpendicular external field [3].

An unusual central flux penetration with increasing the magnetic field (row 2 and 3 of figure. 4) leaves a cylinder of field (bright contrast) within a still field-depleted ring near the edge (dark contrast) that has lower energy than before flux entry. This central flux entry occurred at place of one or more of the grain boundaries that are visible even through the machine marks on the weld samples 4 and 5.

Fig. 6 schematically shows how the flux nucleates in the central part of weld samples when magnetic field slowly increases. Such flux penetration in the weld sample may also be triggered by in-plane components H_x of the magnetic field due to the strong demagnetization factor in perpendicular field resulting in distortion of the magnetic lines around the sample. An example of magnetic fields around rectangular sample in perpendicular field is shown in Fig. 7. Note that H_x has the same direction as the RF magnetic field in cavity wall and consequently these topology influenced perturbation show how nucleation of flux in the sample center may be triggered by surface irregularities.

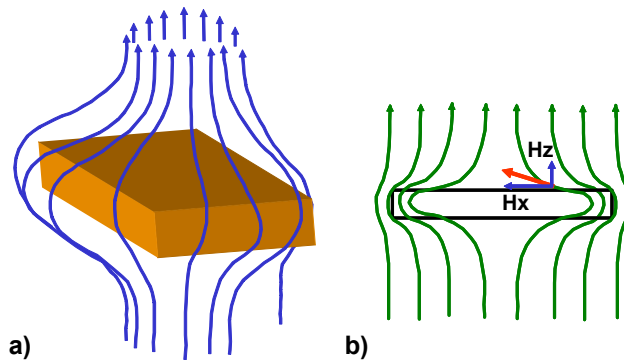


FIGURE 6. a) Schematic pattern of external magnetic field distortion due to demagnetization factor and b) distribution H_x and H_z components.

Surface topology measurements made using a Zygo interferometric light microscope on the weld sample in Figure 7 (after the second etch showed) than it has a convex surface with steps at the GBs (Fig. 8 a,b). The steps heights were about 10 μm . Comparing the Zygo optical and MO images clearly shows that there is a very good correlation between the surface of the weld sample and the MO image (Fig.8 c) with central flux penetration. It is clear that surface topology has an impact on flux penetration in the perpendicular magnetic field when the demagnetization factor is very strong.

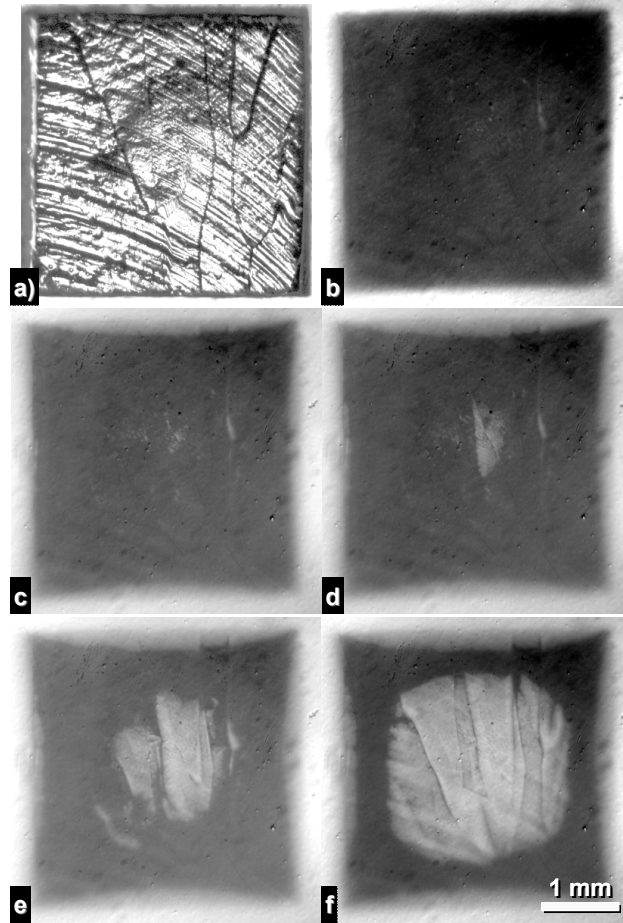


FIGURE 7. MO images of the central flux penetration. a) surface of weld sample: big grains and machine marks are clearly visible, b-f) magneto-optical images at $T=6$ K taken sequentially after magnetic field slowly increase in series to: 32, 52, 54, 56, 60 mT.

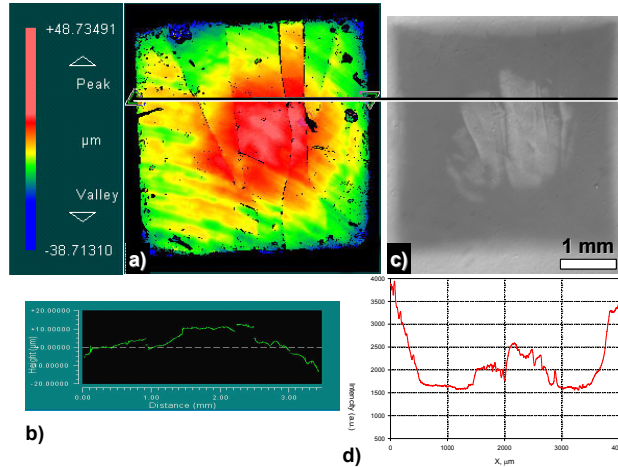


FIGURE 8. a) Surface topology map of weld sample taken by Zygo microscope showing the convex shape; and b) surface profile taken along marked line shows 10 μm steps at GBs; MO images c) with central flux penetration taken at $T = 6 \text{ K}$ and $H=48 \text{ mT}$ and intensity profile along marked line show good correlation with “dome” surface.

Using a split magnetic coil we also applied an external field H_{in} in the in-plane direction in order to investigate the role of topology on flux distribution. Fig. 9 depicts the perturbation of magnetic flux on surface steps when horizontal field was applied in direction shown by the arrow. The in-plane field magneto-optical data reveal the exact field profile as it is found on top of the topological features, in this case the steps

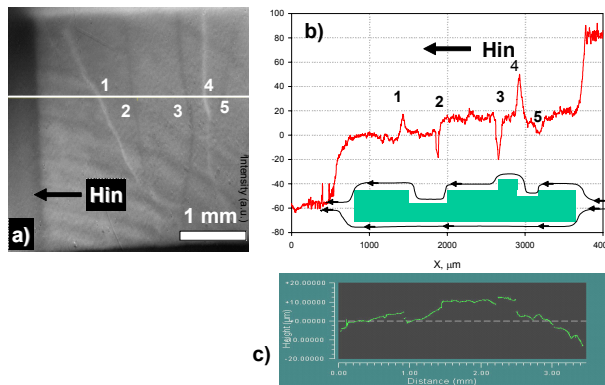


FIGURE 9. Comparison: a) Magneto-optical image taken in in-plane field 60 mT and $T = 6 \text{ K}$; b) intensity and schematic surface profiles along marked line; c) surface profile by interferometric microscope.

between the large grains of the weld region. The intensity profile taken along white line on MO image shows maximum perturbation of in-plane field on steps 2-4, which are about 10 μm high. Such perturbations can lead to enhancement of field on surface steps above first field penetration H_{c1} and can trigger the early flux penetration during RF operation. Even the penetration of small numbers of flux lines into the steps can cause the non-uniform thermal breakdown on cavity surface known as hotspots. Such penetration can depress the Q-factor and cause cavity quench [9, 10]. To make clear the role of GBs and topology on the central flux penetration and its instability we

sequentially polished the weld sample first mechanically and then by BCP and imaged by MO after each procedure (Fig. 10). We have very flat surface after mechanical polishing with $0.05\ \mu\text{m}$ alumina suspension, but traces of GBs are still visible while machinery marks (grooves) disappeared. The 7-minute BCP developed again small steps at the GBs, which were only a few microns high. Fig. 10 compares MO images before and after polishing by mechanically and BCP. The central flux penetration disappeared after mechanical polishing and did not appear even after BCP, when small steps between grains appeared again. The 7-minute BCP removed most of the surface defects created during mechanical polishing, but also created small steps at the GBs. The MO image in ZFC regime showed a mixture of regular and dendritic flux, instead of central penetration. The in-field measurement did not show disturbance of the Hx component when the step height was less than $10\ \mu\text{m}$. Further MO imaging using in-plane field can help us estimate the field enhancement factor at GB steps.

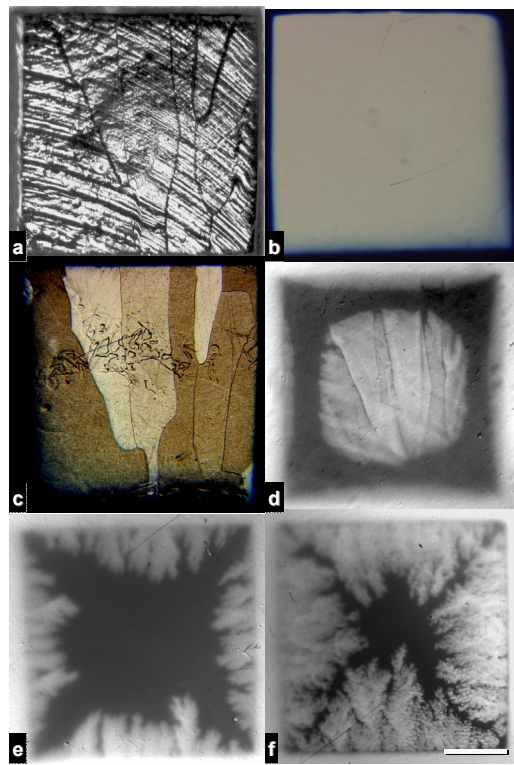


FIGURE 10. Comparison optical (a,b,c) and MO (d,e,f) images of weld sample before and after mechanical polishing and BCP: a) optical surface with $10\ \mu\text{m}$ steps; b) no steps on surface after mechanical polishing; c) grain structure and small steps are visible after BCP. Three MO images taken in ZFC $T = 6\ \text{K}$ and $H = 60\ \text{mT}$.

Very Large Grain Size Nb Sheet

Fig 11a shows one portion of the $1.8\ \text{mm}$ thick sheet which has three grains and two grain boundaries. The grain sizes in the investigated sheet were over a few centimeters [2, 12].

Solid lines show traces of GBs on the top of sheet while dotted lines present traces of GBs on the bottom. By superimposing traces from both sides of the sheet we can

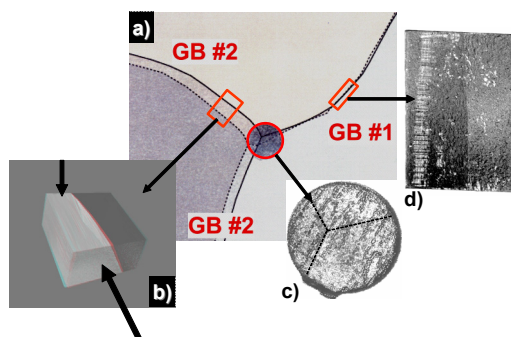


FIGURE 11. a) Detail of as-received ingot slice showing bi and tri-crystal areas, where two rectangular b), d) and one c) disc-shape samples were cut. Sample b) has a 35° declined GB, d) has perpendicular GB and c) has triple-point where all GB have angle with surface.

clearly show where GBs twist out of the normal plane. GB #1, which is almost perpendicular to both surfaces, twists in the vicinity of the triple point, where it meets the GB #2. In contrary, GB #2 has a 30-35° angle to the surface. Orientation imaging microscopy quantified the crystallographic misorientation angles between adjacent grains at larger than 17° (GB #1) and 36° (GB #2). Two rectangular and one circular samples were cut from the 1.8 mm sheet (Fig. 11 b,c and d). Sample b) has a GB(#2) tilted at a 35° to the surface, while the disc-shaped sample c) contains the triple point of GB #1 and #2 and only sample d) has GB #1 normal to surface. ZFC and FC regimes were performed in the direction perpendicular to surface.

Initially we studied the samples with a thickness of 1.8 mm in an as-received slice of Nb with residual cold work on surface. MO imaging showed premature flux penetration at a perpendicular GB on both sides of sample. MO and magnetization measurement revealed that penetration into the GB occurs at fields below H_{c1} . Some samples were subsequently reduced in thickness to 0.3 mm using a diamond saw, thus reducing the grain displacement from topside GB to bottom that had been caused by the grain boundary twisting through the sample. Each of the sliced samples had one as-received surface, while opposite side was polished after being cut by the diamond saw. Both sides of the thinner sample showed clearer and symmetric flux penetration in those GBs than in the as-received thicker sample.

Fig. 12 presents optical and MO images comparing the trapped flux behavior of three types of bi-crystal samples. MO imaging on the as-received surface in perpendicular field did not detect flux perturbation due to GBs in rectangular sample (Fig. 12 a and b), with 35° GB#2 and in the circular (Fig.12 c,d) with the triple-point. However in the 0.3 mm thick sample on polished surface Fig. 12e,f) with perpendicular GB#1 dark contrast at the GB is clearly visible. The dark contrast indicates that the flux escaped from the perpendicular GB. The evidence for the weakness of GB #1 is presented in the MO image in the ZFC regime in Fig. 13a. This image is taken on the polished side of the sample. It is clearly visible that the flux penetrates into the GB faster than in the grains. The current reconstruction from the MO image in Fig. 13b demonstrates that the trajectory of the stream lines of the induction current have a strong perturbation at the GB. That also indicates that the GB is a barrier to current flow. Our initial resistivity measurement also indicates the weakness of the perpendicular GB (#1). This result is the first direct evidence of depressed superconductivity at a Nb grain boundary.

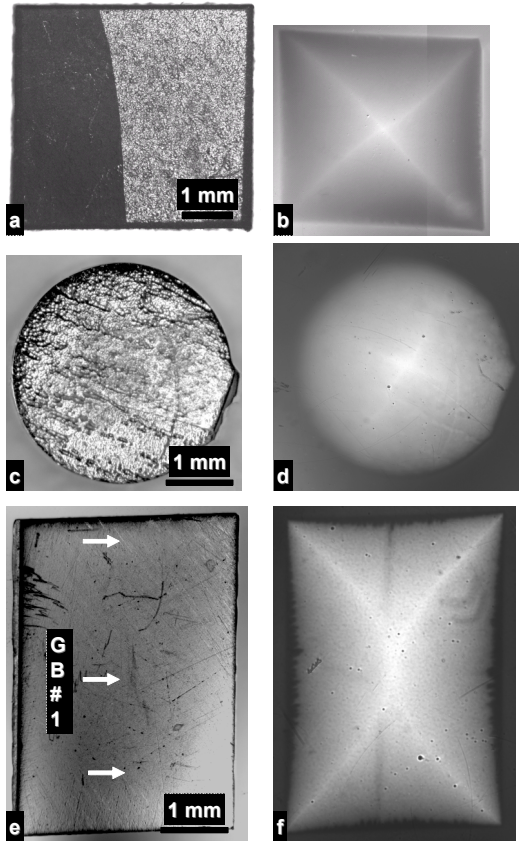


FIGURE 12. Optical surfaces a), c) and e) and MO images b), d) and f) showing trapped flux in these samples with different GBs. Sample a) has a 35° declined GB, c) has triple-point where all GBs deviate from perpendicular to the surface and e) has perpendicular GB. f) The magnetic flux escaped only from the perpendicular GB (dark vertical trace).

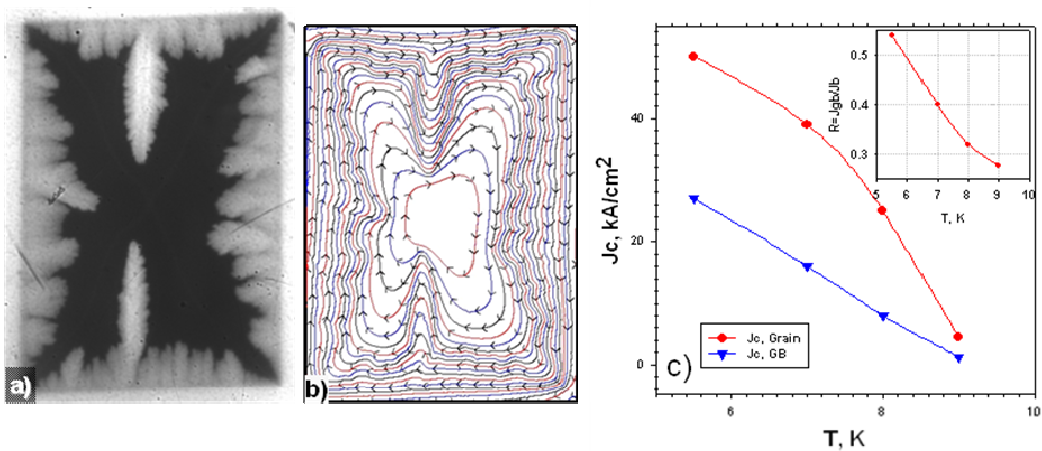


FIGURE 13. a) Magneto-Optical image of flux penetration and b) current distribution on perpendicular GB taken at $T=6$ K and $H=80$ mT., c) calculated from MO images critical current in Nb grains and across GB (inset is the ratio of critical current in grains to critical current across GB).

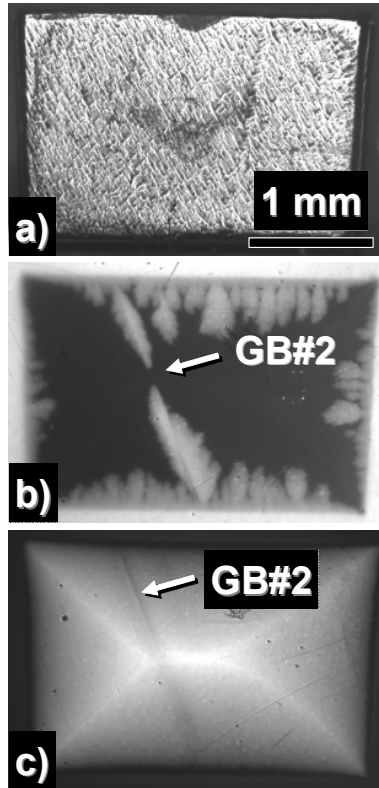


FIGURE 14. a) Light microscope image of the surface of Nb sample b) showed in Fig 11, when it was rotated by 90° . The location of the GB is not visible after diamond saw cutting. The GB is normal to surface. MO images taken at $T=6$ K in ZFC b) $H=32$ mT and FC c), when $H=120$ mT reduced to zero. The weakness of the GB is clearly visible in both MO images.

As was mentioned above, the misorientation angles between adjacent grains for GB #2 is larger than for GB #1, but flux did not enter in the declined GB #2. Is it due to orientation of the external field to the plane of the GB? In a further experiment, bi-crystal GB #2 (Fig. 11b) was rotated by 90° and re-sliced to the 0.3 mm thickness so that the GB now ran perpendicular to the examined surface. The long arrow in Fig. 11b indicates the new direction of the magnetic field in the rotated sample. The plane of the GB is now normal to the top surface (indicated by long arrow) and parallel to the external field. Fig. 14a shows the light microscope image of the sample surface after being cut by the diamond saw. The sample surface was rough ground and the GB #2 was not visible on the surface under conventional light microscopy. However the MO image shows that the flux penetrates at the GB #2 across the entire sample width (Fig. 14b). Flux enters into the GB much faster than into the grains. The FC image in Fig. 14c also demonstrates the weakness of the GB, as magnetic flux escapes from the GB, leaving a sharp dark trace along the GB. The GB is a barrier to shielding current, which circulates inside the sample due to the trapped flux. The same flux behavior was observed on the mechanically polishing surface.

Our studies show that this flux penetration into the GBs with planes parallel to the magnetic field does not relate to surface topology. Even much larger topological features like an artificial notch created on the surface a Nb single crystal (Fig. 15) does not disturb the magnetic flux. Fig. 16 also confirms the absence of a groove at GB #1 so even a strong in-plane field directed perpendicular to the GB does not create MO contrast. However, GB #1 admits in-plane magnetic field parallel to the GB. Dark and bright triangular contrasts demonstrate flux entry into GB #1. This implies that GB weakness will occur in randomly oriented Nb sheet using for RF cavities, so the RF

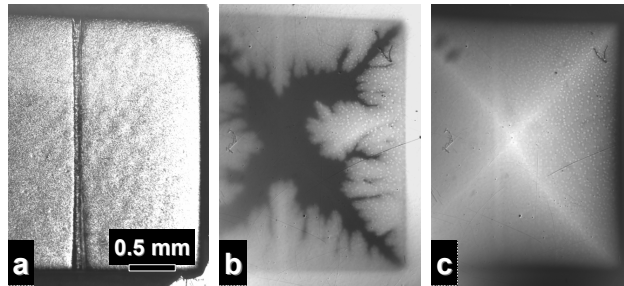


FIGURE 15. Light microscope a) and MO images taken at $T=6$ K in ZFC b) $H=40$ mT and FC c), when $H=80$ mT reduced to zero on single Nb with an artificial notch. There is no magnetic flux distortion due to the notch.

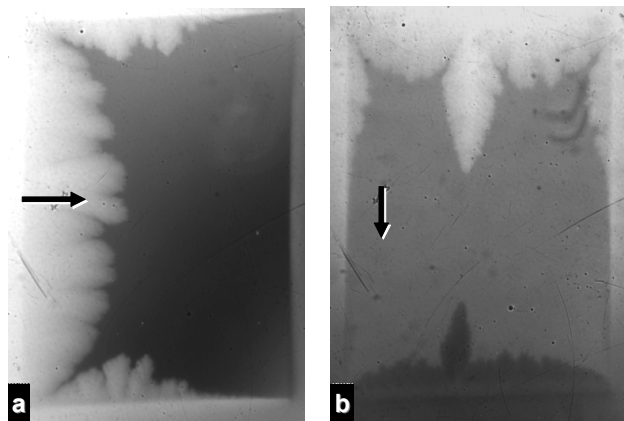


FIGURE 16. MO images taken with in-plane field applied in two perpendicular directions (see arrows). The sample surface showed in Fig. 12 e) has normal GB. a) The 300 mT in-plane field generated using a permanent magnet did not show field perturbation on perpendicular GB. b) magnetic flux enters to GB when the in-plane field is parallel to the GB.

in-plane magnetic field can easily penetrate and cause Q-factor drop during operation. Fig. 17 demonstrates that slightly increasing temperature to 8.3 K can dramatically change the pattern of flux penetration for in-plane field applied in different direction. The flux behavior is unstable and splits into striped domains.

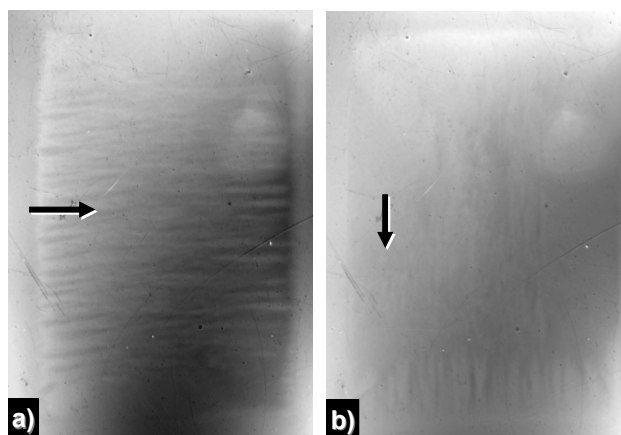


FIGURE 17. ZFC MO images a) and b) taken in in-plane field $H=64$ mT for two different directions show flux instabilities when temperature slightly increases to 8.3 K.

SUMMARY

Using Magneto Optical imaging we have shown that the surface topology in polycrystalline samples with big grains has significant impact on the behavior of flux penetration while we have not seen any evidence of flux penetration along GBs. This result may be due to the more complex geometry of the grain boundaries in these samples. In contrast, the as-received large grain slice allows us to look at individual GBs that traverse the entire slice. In this case the MO imaging reveals a weakness of the grain boundaries, which is not explained by topology. However, that weakness is only revealed when the plane of grain boundary is close to parallel with the applied magnetic field.

ACKNOWLEDGEMENTS

We would like to thank Peter Kneisel and Ganapati Rao Myneni and their colleagues at TJNL for providing the Nb slices.

The work at the Applied Superconductivity Center was supported by US DOE-LCRD under grant DE-FG02-05ER41392 and supplemental support was provided by Fermi lab under PO 570362.

REFERENCES

1. A. A. Polyanskii, P. Bauer, P.J. Lee, C. Boffo, L. Bellantoni, H. Edwards, A. Gurevich, M. Jewell, D. Larbalestier, G.K. Perkins, A. Squitieri., *Pushing the Limits of RF Superconductivity Workshop*, edited by Kwang-Je Kim and Catherine Eyberger, Argonne National Laboratory 2005, pp. 84-93. <http://www.aps.anl.gov/conferences/RFSC-Limits/ReadingMaterial.html>
2. P. J. Lee, A. A. Polyanskii, A. Gurevich, A. A. Squitieri, D. C. Larbalestier, P. C. Bauer, C. Boffo, H. T. Edwards, *Physica C* 441(1), 126–129 (2006).
3. A. A. Polyanskii, A.A. Squitieri, M.C. Jewell, P.J. Lee, A.,Gurevich, D.C. Larbalestier, P. Bauer, L. Bellantoni, C. Boffo.. *12th International Workshop on RF Superconductivity*, Cornell University, Ithaca, NY July 10-15, 2005
4. Gmelin, *Handbuch der anorganischen Chemie*, Vol. 49(Nb), Springer, Berlin, 1970.

5. P. Kneisel, *Proceedings of the Workshop on RF Superconductivity*, edited by M Kuntze (Ed.), Vol. I + II, KFK, Karlsruhe, 1980, p. 27, KFK-3019.
6. K. Saito et al., *Proceedings of the 8th Workshop on RF Superconductivity*, edited by V. Palmieri, Vol. I + II, INFN, Abano terme, 1997, pp. 759-813.
7. L. Lilje et al., *Nucl. Instr. And Meth. A* 516 (2-3) (2004) 213.
8. P. Kneisel, *Proceedings of the 9th Workshop on RF Superconductivity*, edited by F. Krawczyk (Ed.), Vol. I + II, LANL, Santa Fe, 1999, pp. 77-91.
9. A. Gurevich, *12th International Workshop on RF Superconductivity*, Cornell University, Ithaca, NY July 10-15, 2005.
10. A. Gurevich, *Appl. Phys. Letters* **88**, 012511-3, (2006).
11. K. Saito, *Pushing the Limits of RF Superconductivity Workshop*, Argonne National Laboratory, September 22-24, 2004. Argonne National Laboratory Report ANL-05/10, edited by Kwang-Je Kim and Catherine Eyberger, <http://www.aps.anl.gov/conferences/RFSC-Limits/ReadingMaterial.html>
12. P. Kneisel, G. Ciovati, G.R.Myneni, J. Sekutowicz, T. Carneiro, *12th International Workshop on RF Superconductivity*, Cornell University, Ithaca, NY July 10-15, 2005.
13. A. A. Polyanskii, D. M. Feldmann, and D. C. Larbalestier, "Magneto-Optical Characterization Techniques," in *"The Handbook on Superconducting Materials,"* edited by David Cardwell and David Ginley, Institute of Physics UK , pp. 1551-1567, 2003